Self-interaction-free approaches for self-consistent solution of the Maxwell-Liouville equations

Alexei Deinega and Tamar Seideman
Department of Chemistry, Northwestern University, 2145 Sheridan Road, Evanston, Illinois 60208-3113, USA
(Received 23 September 2013; published 3 February 2014)

We propose two complementary approaches for solution of the coupled Maxwell-Liouville equations within the finite-difference time domain (FDTD) framework. The two methods are specifically designed to eliminate self-interaction, which often appears spuriously in simulation of the coupled Maxwell-Liouville equations, and hence can be used for modeling of single as well as ensembles of quantum emitters (such as molecules or quantum dots) in an arbitrary dielectric environment. One approach borrows from the familiar total field–scattered field technique that has been applied in the past in a different context. The second recognizes an opportunity to average over the electric field at a set of specifically chosen points around the quantum emitter. The methods introduced are applied to two problems of growing current interest that also present useful test cases. One is the modeling of spontaneous emission, where comparison with an analytical solution illustrates the accuracy and efficiency of the methodology. The second is quantum-emitter-induced transparency in a resonator formed by two gold ellipsoids, where Fano interferences suggest interesting potential applications.

DOI: 10.1103/PhysRevA.89.022501 PACS number(s): 33.90.+h, 42.50.Ct, 73.20.Mf, 78.67.−n

I. INTRODUCTION

The optical properties of hybrid systems that combine quantum emitters (such as quantum dots or dye molecules) and metal nanoparticles are of much current interest. Metal nanoparticles exhibit strong excitations in the form of localized surface plasmons characterized by large field enhancement near the nanoparticle [1–3]. In addition, the local density of photonic states can be greatly altered in the presence of the nanoparticle. As a result, placing a nanoemitter in proximity to a metal nanoparticle significantly changes its spontaneous emission rate [4–6]. The electromagnetic interaction of plasmons and quantum emitters can lead to new physical effects, which are particularly evident for semiconductor quantum dots (QDs), since they have large dipole moments and good photostability [7]. Tuning the exciton frequency of the QD to the frequency of a plasmon resonance can strongly modify the optical response of the whole system. Interference of the applied electric field and the field generated by the QD leads to asymmetric Fano shapes in the metal nanoparticle absorption spectrum [8,9] and to quantum-dot-induced transparency [10–14]. It was predicted that application of a moderately intense incident field (in the 1 kW/cm^{-2} range) can result in Rabi flopping [15,16], modify the absorption line shape, and lead to optical bistability, due to strong self-interaction of the QD (that is, feedback through the nanoparticle) [17].

A self-consistent approach to model all these effects requires simulation of a coupled system of the Maxwell and Liouville equations. In such framework the quantum state of the emitter is described by a density matrix $\hat{\rho}$ whose evolution is given by the Liouville equation,

$$i\hbar\frac{\partial\hat{\rho}}{\partial t} = [\hat{H},\hat{\rho}] - i\hbar\hat{\Gamma}\hat{\rho}, \tag{1}$$

$\hat{H}$ being the Hamiltonian, and $\hat{\Gamma}$ a superoperator describing decay of excited states and dephasing. The Hamiltonian includes a time-independent free component $\hat{H}_0$ and an interaction with an electromagnetic field $\mathbf{E}(t)$,

$$\hat{H}(t) = \hat{H}_0 - \hat{\mathbf{p}}\cdot\mathbf{E}(t), \tag{2}$$

where $\hat{\mathbf{p}}$ is the dipole moment operator of the quantum system.

The evolution of the electromagnetic fields, **E** and **H**, is governed by Maxwell's equations,

$$\mu\frac{\partial\mathbf{H}}{\partial t} = -\nabla\times\mathbf{E}, \tag{3}$$

$$\varepsilon\frac{\partial\mathbf{E}}{\partial t} = \nabla\times\mathbf{H} - \frac{\partial\mathbf{P}}{\partial t}, \tag{4}$$

where μ is magnetic permeability, ε is dielectric permittivity, and **P** is the macroscopic polarization. For continuously distributed emitters (ensemble of atoms or molecules), **P** reads as

$$\mathbf{P} = n_a\langle\mathbf{p}\rangle, \tag{5}$$

where n_a is the atomic (molecular) density, and $\langle\mathbf{p}\rangle = \mathrm{Tr}(\hat{\rho}\hat{\mathbf{p}})$ is the expectation value of a dipole moment. For a single emitter (one molecule or quantum dot) the polarization is given by [18,19]

$$\mathbf{P} = \langle\mathbf{p}\rangle\delta(\mathbf{r}-\mathbf{r}_0). \tag{6}$$

The system of Maxwell (3), (4) and Liouville (1) equations should be solved self-consistently, since the electric field **E** determined through Maxwell's equations influences the Liouville equation as an argument, see (2), while the dipole moment $\langle\mathbf{p}\rangle = \mathrm{Tr}\,(\hat{\rho}\hat{\mathbf{p}})$ enters Amper's law (4) through the polarization **P**.

At large (compared to the size of the nanoparticle) distances between the quantum emitter and the nanoparticle, solution of Maxwell's equations can be simplified using the nonretarded dipole approximation [8,9,15–17]. In this approximation, the nanoparticle is considered as a static dipole induced by the incident field and the field generated by the quantum emitter. The field produced by the nanoparticle, along with the incident field, enters the Liouville equation for the nanoemitter (1), (2), which can be solved using the rotating-wave approximation. At small distances between the nanoparticle and quantum emitter, the dipole approximation is not applicable, and electric multipole effects should be taken into account [20]. However, the electric multipole expansion has a simple form only for spherical-type particles, and is applicable only for particles

with lengths much smaller than the incident wavelength. Thus, a complete model for the considered system requires a full electromagnetic calculation, including retardation.

Recently, it was proposed to apply the boundary element method to describe the interaction of a QD with a metal nanoparticle [21]. Alternatively, one can use the finite-difference time domain (FDTD) method [22]. In the FDTD framework, the temporal Maxwell's equations are solved on a space-time grid, which makes this method particularly suitable for modeling of time-dependent processes and applicable to structures of arbitrary geometry. The first FDTD simulations of the Maxwell-Liouville equations were initiated by Ziolkowski for two-level atoms in one dimension [23]. Subsequently, this approach was extended to higher dimensions and used in different applications [24–28]. The approach proposed by Ziolkowski is based on an iterative predictor-corrector scheme, which makes it time consuming. In addition, it is not straightforward to generalize this approach to treat multilevel systems. A more efficient technique is based on decoupling of the Liouville equation from the Maxwell equations, which results in improved numerical efficiency [29–34]. Alternatively, one can solve the rate equations for the population density [35–40].

The proposed FDTD schemes were designed for continuously distributed atoms (molecules) (5), and certain corrections should be made to model a single quantum emitter (one molecule or quantum dot). In this case, the polarization is given by (6), and the quantum emitter should be simulated as a point current source. The electric field produced by a point source in the FDTD scheme is nonzero at the position of the source. Therefore the electric field in the Hamiltonian (2) contains a field produced by the emitter itself (we will discuss the consequences of this effect at the end of the next section). To avoid such a self-interaction, it was proposed to split the total electric field into two parts: the primary radiation of a quantum emitter and the field resulting from everything else. Both fields are simulated using FDTD, while the Hamiltonian (2) includes only the second part [18,19,41]. This approach was applied to model plasmon transfer across a pair of gold nanoparticles separated by a single molecule. The drawback of this approach is the necessity to store and update arrays for both electric fields. It becomes inefficient when considering more than a single quantum emitter, since the number of components of the electric field increases, as well as the required memory and number of computer operations.

In this paper we propose two approaches to solve the coupled Maxwell-Liouville equations for a single quantum emitter (or any discrete number thereof). The first approach is based on a field-partitioning concept akin to the familiar total field–scattered field technique [22] but applied in a different manner with the result of excluding the primary radiation of the emitter from its position. In the second approach, the field applied to the quantum system via Eq. (2) is averaged over a specifically chosen, symmetry-adapted set of points. This averaged field is shown to exclude all self-interactions. The two approaches are complementary in application, in the sense that the second is easier to implement but less accurate compared to the first one. We apply the two methodologies to two problems of growing fundamental and practical interest that also present suitable test cases, namely the calculation of spontaneous emission rates and the response of a hybrid system consisting of a single quantum emitter placed in the gap between a pair of gold ellipsoids.

The paper is organized as follows. In Sec. II, we give detailed descriptions of both methodologies. In Sec. III, we present and discuss the results of their application, and in the final section we summarize our conclusions, pointing to avenues for future work.

II. METHOD

A. Field-partitioning approach

Within the FDTD framework, electromagnetic sources are commonly simulated using a current term in Ampere's law (4). A numerical map of a point source (6) on an FDTD grid corresponds to nonzero current at a single FDTD grid point. The electric field produced by such a numerical source is nonzero at the grid point itself. This leads to a problem of coupling between the Maxwell (3), (4) and Liouville (1), (2) equations, since the latter should not contain the primary field generated by source. In other words, we need to separate the primary source field from the external field at the position of the source.

To solve this problem, we borrow from the total field–scattered field (TF-SF) technique [22], commonly applied in a different context in FDTD methods. This technique is based on a known property of Maxwell's equations; namely, the evolution of the electromagnetic fields in a closed sourceless volume is determined by the fields at the boundary of this volume. Within the TF-SF framework, one divides the computational volume into the total field (TF) and scattered field (SF) regions. The discretized Maxwell equations in the SF region are solved for the scattered field $\mathbf{E}_{\mathrm{sc}}$, which is the difference between the total field $\mathbf{E}$ and the known unscattered incident field $\mathbf{E}_0$,

$$\mathbf{E} = \mathbf{E}_0 + \mathbf{E}_{\mathrm{sc}}. \tag{7}$$

The TF region contains scattering objects and is where the discretized equations for the total field $\mathbf{E}$ are solved. The discretized equations have exactly the same form in both regions, except at grid points adjacent to the border between the TF and SF regions. The equations corresponding to these points contain fields from different regions and should be modified with correction terms that include the incident field $\mathbf{E}_0$. A detailed description of the TF-SF technique can be found in [22].

The TF-SF technique is usually used in FDTD to generate an incident plane wave. Some modification of this technique is required to simulate periodic structures for the case of oblique incidence. In this case, the incident field can be written as the signal evolution recorded during a preliminary FDTD simulation [42,43] or a packet of plane waves with fixed in-plane wave vector [44,45]. The last modification is used within the hybrid FDTD transfer matrix method as well [46]. The TF-SF concept can be also applied in a multigrid FDTD approach, to transfer fields between inserted (intersected) grids [47–49].

The present work introduces a rather different TF-SF concept. Here the TF-SF border surrounds a virtual point source. The SF region is the area confined by this border, whereas the TF region is the open area outside the TF-SF

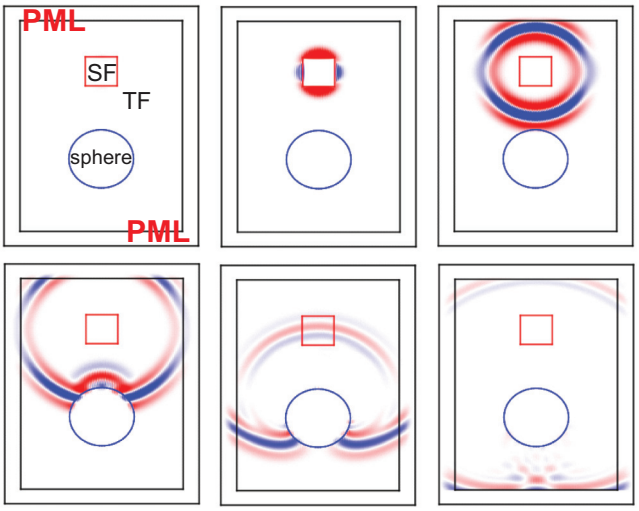

FIG. 1. (Color online) The field-partitioning method: evolution of the electric field component parallel to the dipole moment, which is horizontally directed. The TF-SF boundary (shown in red) has a form of a box, the interior of which consists of the SF region whereas the open area outside the box is the TF region. The generated dipole radiation (8), (9) propagates outside the TF-SF border into the TF region. Part of this radiation is reflected back from a conductive sphere (blue).

border (Fig. 1). The incident field is given by an analytical expression for the dipole radiation [4] (we assume the case of a nonmagnetic medium),

$$\mathbf{E}_0(\mathbf{r}) = \frac{1}{4\pi\varepsilon_0}\left[\frac{3\mathbf{e}_r(\mathbf{e}_r,\mathbf{p})-\mathbf{p}}{n^2r^3} + \frac{3\mathbf{e}_r(\mathbf{e}_r,\dot{\mathbf{p}})-\dot{\mathbf{p}}}{cnr^2} + \frac{\mathbf{e}_r(\mathbf{e}_r,\ddot{\mathbf{p}})-\ddot{\mathbf{p}}}{c^2r}\right], \quad (8)$$

$$\mu_0\mathbf{H}_0(\mathbf{r}) = \frac{n}{c}\mathbf{e}_r \times \left[\mathbf{E}_0(\mathbf{r}) + \frac{\mathbf{p}}{r^3}\right], \quad (9)$$

where r is the distance from the dipole to the observation point, $\mathbf{e}_r = \frac{\mathbf{r}}{r}$ is a unit vector in the direction of the observation point, $\mathbf{p}$ is the value of the dipole moment at time $(t - n\mathbf{r}/c)$, we use overdots to signify first or second time derivatives, and n is the refractive index of the external medium. The TF-SF border generates dipole radiation propagating outside into the TF region, whereas the SF region contains only external field from other sources, or dipole field scattered from other objects (Fig. 1). Thus, the field simulated at the position of the point source does not contain a spurious primary dipole radiation $\mathbf{E}_0$ and can be applied to the quantum system through the Hamiltonian (2). For solution of the Maxwell-Liouville equations, the dipole moment is given as $\mathbf{p} = \langle\mathbf{p}\rangle = \mathrm{Tr}(\hat{\rho}\hat{\mathbf{p}})$. Our approach allows the simulation of several sources (e.g., quantum dots) using multiple independent TF-SF borders.

Note that the radiation produced by the point source is significantly distorted by the FDTD rectangular mesh in the close proximity to the source. In other words, the analytical expression for the dipole radiation (8), (9) differs from its numerical analog at the grid points close to the source (this is common problem of simulations of evanescent fields in FDTD [46]). Therefore the size of the SF region should not be too small; otherwise use of the analytical expressions (8), (9) for the incident field will result in spurious numerical signal propagating in the SF region. In our simulations we use a box-shaped SF region with the size $a \geqslant 7\Delta r$, where Δr is the mesh step. In principle it is possible to use a smaller SF region but this would require use of a numerical representation of the dipole field instead of (8), (9). Such numerical field can be possibly found by modification of the technique described in [50]. We remark that our partitioning approach does not require placement of the virtual source exactly at a grid point. The source location can be chosen arbitrarily within the SF region, since information about this is only contained in the values of r and $\mathbf{e}_r$ in (8), (9).

B. Symmetry-adapted averaging approach

In this subsection we introduce a complementary method to that developed in the previous subsection to separate the primary field $\mathbf{E}_0$ produced by a point source from the external field $\mathbf{E}_{\mathrm{sc}}$. The method is not as accurate as the one presented above but has the merits of elegance and simplicity. Consider a sphere centered at the position of a point source $\mathbf{r}_0$. If the radius of this sphere R is small enough, the external field is almost constant within the sphere, whereas the source radiation can be approximated by the first term in (8), which corresponds to the field of a static dipole (the subsequent terms are small compared to the first one, due to the lower power of r in denominator). It can be readily shown by direct integration that

$$\int_S [3\mathbf{e}_r(\mathbf{e}_r,\mathbf{p}) - \mathbf{p}]\, dS = 0 \quad (10)$$

for arbitrary $\mathbf{p}$. Therefore

$$\frac{1}{4\pi R^2}\lim_{R\to 0}\int_S \mathbf{E}\, dS = \frac{1}{4\pi R^2}\lim_{R\to 0}\int_S \mathbf{E}_{\mathrm{sc}}\, dS = \mathbf{E}_{\mathrm{sc}}. \quad (11)$$

Note that expression (11) corresponds to the electric field averaged at the surface of the sphere (dS is a scalar). This is not the same as the electric flux through this surface, which clearly vanishes according to Gauss's law (the total charge of the dipole inside the sphere is zero). The averaged field (11) does not contain the primary dipole $\mathbf{E}_0$ radiation and can be applied to the quantum system through the Liouville equation.

For numerical reasons, it is preferable to calculate the average of the electric field over some symmetric set of points, rather than take an integral (11). Consider, for instance, the set of six points $\mathbf{r}_0 \pm a\cdot\mathbf{e}_x$, $\mathbf{r}_0 \pm a\cdot\mathbf{e}_y$, $\mathbf{r}_0 \pm a\cdot\mathbf{e}_z$, where $\mathbf{e}_i$ are unit vectors in the directions of the coordinate axes, and a is an arbitrary number (Fig. 2, left). The near field of an arbitrarily directed dipole, $\mathbf{p}$, averaged over this set of points vanishes, since

$$\sum_{i=x,y,z}[3\mathbf{e}_i(\mathbf{e}_i,\mathbf{p}) - \mathbf{p}] = 0. \quad (12)$$

This is readily seen for the case where $\mathbf{p}$ is parallel to one of the coordinate axes ($\mathbf{p} = \pm\mathbf{e}_i$), and since an arbitrary $\mathbf{p}$ can be represented as a sum of its three projections it holds quite

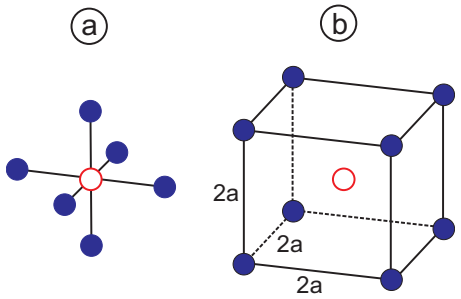

FIG. 2. (Color online) The arithmetic average of the dipole near field vanishes if taken at the centers of sides (a) or at the vertices (b) of a cube centered at the dipole position (empty circle).

generally. Therefore, the scattered field can be estimated as

$$\mathbf{E}_{\rm sc}(\mathbf{r}_0) \approx \frac{1}{N}\sum_i \mathbf{E}(\mathbf{r}_i), \tag{13}$$

where N is the number of points [6 in the case considered in Fig. 2(a)], and $\mathbf{r}_i$ are their coordinates. Another possible set of points are the 8 vertices of a cube of size $2a$ that is centered at the position of the dipole: $\mathbf{r}_0 \pm a\cdot\mathbf{e}_i \pm a\cdot\mathbf{e}_j, i \neq j$ [Fig. 2(b)].

As discussed above, the dipole field is distorted by the FDTD rectangular mesh in close proximity to the location of the dipole. Therefore, its arithmetic average will not vanish if a is too small, including only a few mesh steps (moreover, it will depend on the frequency of the dipole radiation). Clearly, one cannot choose a less than a mesh step, since in this case numerical interpolation of the electric field will involve its value at the location of the dipole. At the same time, for too large a value of a, the arithmetic average of the field $\mathbf{E}_{\rm sc}$ will differ from its value at the position of the dipole. Further, the last radiating term in (8) becomes dominant for large a (in the far zone), which leads to nonzero averaged dipole field, since $\sum_{i=x,y,z}[\mathbf{e}_i(\mathbf{e}_i,\mathbf{p})-\mathbf{p}] \neq 0$; compare with (12). Thus, there is an optimal range of values of a which is transferable (independent from the simulated geometry).

We compared our approach with the standard way of solving the Maxwell-Liouville equations, where the electric field at a FDTD grid point (which includes the primary radiation produced by this point) enters the Hamiltonian (2). We found that the latter approach can lead to changes in resonant frequencies and/or spectral peak amplitudes. One can observe the effect in a simple simulation of the electromagnetic response of a single quantum emitter driven by an incident field in vacuum (Fig. 3). Below we explain the origin and sign of the numerically observed shift using a simple analytical model. We note that a similar effect was reported in the past in a study of an atomic layer coupled to a plasmonic system [33], where the field used in the quantum solution was taken to be of the form

$$\mathbf{E} + \frac{\mathbf{P}}{3\varepsilon_0}, \tag{14}$$

allowing account of dipole-dipole interaction within a single grid cell [51].

Before concluding this section, we introduce an elegant way of confirming that the primary radiation of a single emitter influences its dynamics in the standard approach of simulating

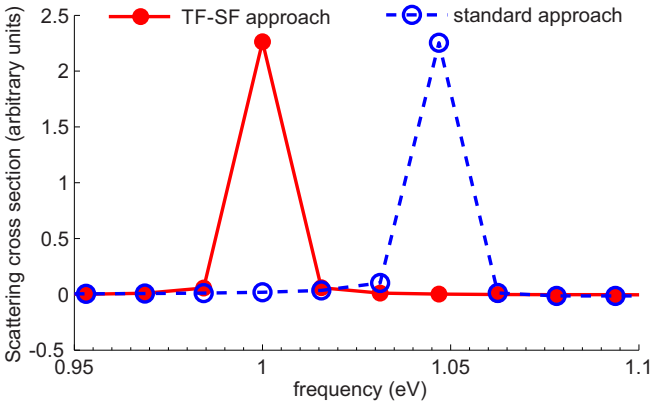

FIG. 3. (Color online) FDTD results for the scattering cross section of a single quantum emitter (transition frequency $\omega_0 =$ 1 eV, dipole moment $\mu = 1\,e$ nm, relaxation rates $\gamma = 10^{13}$ s^{-1}, $\gamma^* = 0.5\times 10^{13}$ s^{-1}) subject to an incident light. The mesh step is $\Delta r = 1$ nm. Using the standard approach leads to a blueshift of the emitter spectral response.

the Maxwell-Liouville equations. If one changes the sign of the interaction term in (2) from negative to positive, the standard approach becomes unstable and can lead to increase of the excited population even in the absence of an incident applied field (if the dipole moment and relaxation times are not small). This is evidently incorrect, since changing the sign of the interaction term in (2) in the case of a free-space (with no scattering objects) simulation should not influence the dynamics of the emitter.

To explain this effect, we consider the discretized Amper law (4), neglecting the magnetic field, $\varepsilon\frac{\mathbf{E}}{\Delta t} \approx -\frac{\mathbf{P}}{\Delta t}$. The numerical electric field $\mathbf{E}_0$ corresponding to the primary source radiation should be directed oppositely to its polarization $\mathbf{P}$ at the position of the source,

$$\mathbf{E}_0(\mathbf{r}_0) \sim -\mathbf{P}. \tag{15}$$

In the limit of a two-level system and a low-intensity field, the system dynamics can be described by an oscillator model [52],

$$\ddot{\mathbf{x}} + \gamma\dot{\mathbf{x}} + \omega_0^2\mathbf{x} = \frac{e}{m}\mathbf{E}, \tag{16}$$

where $\mathbf{x}$ is oscillator displacement from equilibrium, γ is the dissipation rate, ω_0 is the transition frequency, e is the charge, and m is the mass. The electric field $\mathbf{E}$ includes the numerical field produced by the emitter $\mathbf{E}_0$; see (7). The dipole moment is $\mathbf{p} = e\mathbf{x}$, and the polarization is proportional to the dipole moment via the numerical value of the delta function in (6) (roughly the inverse of a mesh step). Therefore, one can rewrite (15) as $\mathbf{E}_0 = -\alpha\mathbf{x}$, where α is a positive coefficient which depends on the mesh step. Substituting the last equality into (16) results in an increased transition frequency as compared to the correct value ω_0, $(\omega_0^2 + \alpha\frac{e}{m})^{1/2} > \omega_0$. (This explains a blueshift in Fig. 3.) Change of the sign of the interaction term in (2) corresponds to applying a negative α in our oscillator model. If $|\alpha|$ is large enough [corresponding to a large inverse mesh step and numerical value of the delta function in Eq. (6)], the transition frequency becomes imaginary, and the solution to Eq. (16) diverges.

We note that within the approach developed here the field produced by the emitter is excluded from the Hamiltonian (2) and hence the emitter is completely independent from its primary radiation ($\alpha = 0$). Consequently, our results are invariant under change of the sign of the interaction term, as they should be, exhibiting no instabilities.

III. APPLICATIONS

We implemented the methods developed above as a part of the parallel C++ Electromagnetic Template Library (EMTL) [53]. In this section we apply the theory of Sec. II to two problems of rather general fundamental and practical interest, which in addition present useful tests of our methods, namely the calculation of spontaneous emission rates and the problem of quantum-emitter-induced transparency in a plasmonic antenna system.

A. Calculation of spontaneous emission rates

The spontaneous decay rate γ of a source in a dielectric environment is proportional to the average power radiated by the classical oscillating dipole P [4,5],

$$\frac{\gamma}{\gamma_0} = \frac{P}{P_0}, \tag{17}$$

where the subscript "0" refers to free-space values. The spectral dependence of the power P can be calculated within FDTD using the Fourier transforms $\mathbf{j}(\mathbf{r}_0,\omega)$ and $\mathbf{E}(\mathbf{r}_0,\omega)$ at the location of the dipole [54–57],

$$\begin{aligned} P(\omega) &= \tfrac{1}{2}\mathrm{Re}[\mathbf{j}^*(\mathbf{r}_0,\omega)\cdot\mathbf{E}(\mathbf{r}_0,\omega)] \\ &= \tfrac{1}{2}\mathrm{Re}\,[\mathbf{j}(\mathbf{r}_0,\omega)]\cdot\mathrm{Re}\,[\mathbf{E}(\mathbf{r}_0,\omega)] \\ &\quad + \tfrac{1}{2}\mathrm{Im}\,[\mathbf{j}(\mathbf{r}_0,\omega)]\cdot\mathrm{Im}\,[\mathbf{E}(\mathbf{r}_0,\omega)]\,. \end{aligned} \tag{18}$$

The last two terms on the right-hand side of the second equality sign in (18) are nearly equal in magnitude but opposite in sign [55]; hence their sum could be a source of numerical inaccuracy. In addition, application of expression (18) requires placement of the dipole exactly at an FDTD grid point, which is often a limitation. Alternatively, one can calculate the power $P(\omega)$ by integrating over the flux of the Poynting vector, $\mathbf{S}(\omega) = \frac{1}{2}\mathrm{Re}[\mathbf{E}^*(\omega)\times\mathbf{H}(\omega)]$ along a closed surface surrounding the dipole [58]. This approach, however, requires calculation of the Fourier-transformed field at multiple points on this surface.

As discussed above [see (7)], the total field at the position of dipole is

$$\mathbf{E}(\mathbf{r}_0) = \mathbf{E}_0(\mathbf{r}_0) + \mathbf{E}_{\mathrm{sc}}(\mathbf{r}_0), \tag{19}$$

where $\mathbf{E}_0$ is the primary dipole radiation (8) and $\mathbf{E}_{\mathrm{sc}}$ is the field scattered from other objects and revisiting the vicinity of the dipole (we assume that there are no sources other than the dipole). The power radiated by dipole can be written as

$$P(\omega) = P_0(\omega) + P_{\mathrm{sc}}(\omega), \tag{20}$$

where the contribution of the primary field $\mathbf{E}_0$ is equal to the power radiated by a dipole in free space,

$$P_0(\omega) = \frac{|\mathbf{p}|^2}{12\pi\varepsilon_0}\frac{n\omega^4}{c^3}. \tag{21}$$

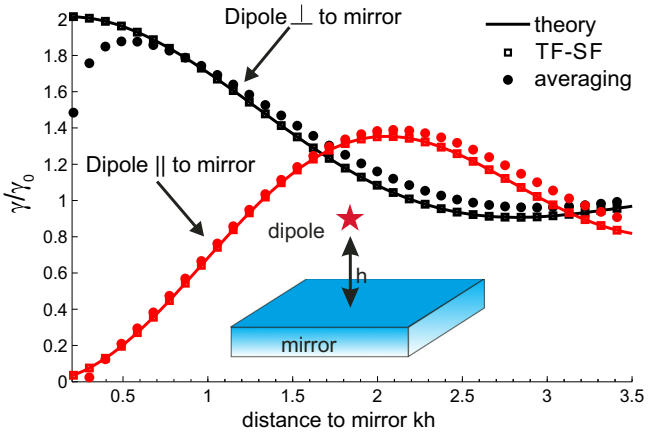

FIG. 4. (Color online) Spontaneous emission decay rate versus the unitless distance parameter kh (where k is the wave vector and h denotes the distance of the quantum emitter from a perfect mirror) for perpendicular and parallel orientations of the dipole with respect to the mirror. The rate is normalized to that in a free space. Results obtained using the field-partitioning approach are in perfect agreement with the analytical results of [59], whereas the symmetry-adapted averaging method yields satisfactory but not full agreement.

The last term in (20) is given as

$$P_{\mathrm{sc}}(\omega) = \tfrac{1}{2}\mathrm{Re}[\mathbf{j}^*(\mathbf{r}_0,\omega)\cdot\mathbf{E}_{\mathrm{sc}}(\mathbf{r}_0,\omega)]. \tag{22}$$

This term (22) can be calculated with knowledge of the scattered field $\mathbf{E}_{\mathrm{sc}}$, which is obtained by applying one of the two approaches described in Sec. II. Within the field-partitioning approach of Sec. II A, $\mathbf{E}_{\mathrm{sc}}$ is the field simulated in the SF region. Within the symmetry-adapted averaging approach of Sec. II B, $\mathbf{E}_{\mathrm{sc}}$ is obtained by averaging the total field over a specifically chosen set of points around the dipole.

To test our approaches we calculate the spontaneous emission rate for an analytically soluble model, namely, a dipole near a perfect mirror. We consider two different dipole orientations: parallel and perpendicular to the mirror (Fig. 4). The distance between the dipole and the mirror is taken to be $h = 30$ and the FDTD mesh step is $\Delta r = 1$ (we use arbitrary units, since in our nondispersive case Maxwell's equations are scaling invariant). The results obtained using our field-partitioning theory, Sec. II A, are seen to be in perfect agreement with the analytical results of [59]. Remarkably good agreement with the analytical results is obtained also using our symmetry-adapted averaging approach, developed in Sec. II B [where we chose, as a simple example, the set of points presented in Fig. 2(a) with $a = \Delta r$]. As anticipated in Sec. II B, the latter approach is seen to be less accurate than the former, yet sufficiently accurate for most purposes, with the merit of being very easy to implement. We remark that differences between the radiated computed field and the analytical expression (8), (9), which may arise from numerical errors, may generate a deviation of the arithmetic average from zero [hence our use of $\approx$ in (13)].

It is useful (and interesting) to note that the primary dipole radiation field $\mathbf{E}_0$ arrives to a chosen set of points with delay d/c, whereas this is not the case for the scattered field $\mathbf{E}_{\mathrm{sc}}$. Hence in applying the symmetry-adapted averaging approach

to expression (22) we implement a phase shift in the averaged field calculation as

$$\mathbf{E}_{\rm sc}(\mathbf{r}_0,\omega) = \frac{1}{N}\sum_i \hat{\mathbf{F}}\left[\mathbf{E}(\mathbf{r}_i, t + d/c)\right], \qquad (23)$$

where N is the number of points [6 and 8 in the cases considered in Figs. 2(a) and 2(b), respectively], $\mathbf{r}_i$ are their coordinates, $d = |\mathbf{r}_i - \mathbf{r}_0|$ (a or $\sqrt{3}a$ in the cases considered in Fig. 2), and $\hat{\mathbf{F}}$ stands for a Fourier transform.

B. Quantum-emitter-induced transparency

In this subsection we consider another problem of more general interest that serves also as a useful test of the methods introduced in Sec. II, namely, the influence of a single quantum emitter (e.g., quantum dot) on plasmon formation in metal nanoparticles.

We solve the Maxwell-Liouville equations following the algorithm described in [31]:

(1) First, the magnetic field **H** is updated according to Faraday's law (3).

(2) Next the electric field **E** is updated using Amper's law (4). The polarization current (6) in Amper's law is calculated using the density matrix $\hat{\rho}$ at the previous time step.

(3) With knowledge of the electric field **E** (stored in memory for the current and previous time step), we update the density matrix $\hat{\rho}$ according to the Liouville equation (1), (2) using a fourth-order Runge-Kutta scheme [60].

Numerical stability is ensured via the requirement that $\mathrm{Tr}(\hat{\rho}) = 1$ at all times.

Our numerical setup is illustrated schematically in Fig. 5. We consider the optical response of a hybrid system consisting of a quantum emitter between two gold ellipsoids embedded in an external medium with refractive index $n = 1.33$. The ellipsoid major and minor diameters are 80 and 30 nm, respectively, and the distance between the ellipsoids is taken to be 15 nm. The incident wave is polarized along the x direction and propagates in the y direction (Fig. 5). We use a mesh step size of $\Delta r = 1$ nm.

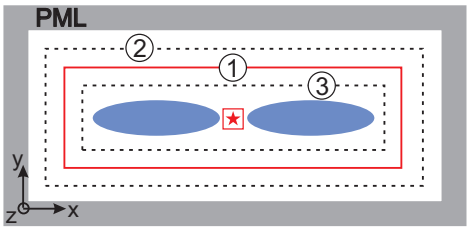

FIG. 5. (Color online) Effects of a quantum emitter (e.g., a single quantum dot) on a plasmonic antenna consisting of a pair of gold ellipsoids. The incident wave is polarized along the x direction and propagates in the y direction. The red box denoted 1 is the TF-SF border for generation of the incident plane wave. Box 2 is the surface applied to calculate the flux of the scattered field. Box 3 is the surface applied to calculate the absorbed electric flux. In a field-partitioning approach (see Sec. II A), we surround a quantum dot (star) by a small (red) TF-SF border that generates a wave of the form (8), (9). In the symmetry-adapted averaging approach (see Sec. IIB), we do not need this additional TF-SF border; therefore, the distance between the ellipsoids (in mesh steps) can be chosen to be smaller.

A quantum emitter (e.g., quantum dot) supports three excitons with optical dipoles parallel to the x, y, and z axes [8]. In the present case, the field at the position of a quantum emitter has only an x component, due to the symmetry of the considered setup (Fig. 5), and hence only the x-oriented exciton contributes. Its dynamics is described by the Liouville equation (1), (2), which can be rewritten as

$$\frac{\partial \rho_{11}}{\partial t} = -\frac{\partial \rho_{22}}{\partial t} = \frac{i}{\hbar}\mu E_x(t)(\rho_{12} - \rho_{12}^*) + \gamma\rho_{22}, \qquad (24)$$

$$\frac{\partial \rho_{12}}{\partial t} = \frac{i}{\hbar}\omega_0\rho_{12} + \frac{i}{\hbar}\mu E_x(t)\,(\rho_{11} - \rho_{22}) - \gamma^*\rho_{12}, \qquad (25)$$

where ω_0 is the exciton transition frequency, μ is the dipole moment, and γ, γ^* are diagonal and off-diagonal dissipation rates (corresponding to population relaxation and phase decoherence, respectively).

We note that Eqs. (24), (25) are inherently nonlinear. However, if the incident intensity is low, the quantum system probability density will reside essentially only in the ground state: $\rho_{11} \approx 1$, $\rho_{22} \ll 1$. Typically $|\rho_{12}|^2 \approx \rho_{11}\rho_{22}$; therefore $\rho_{22} \ll |\rho_{12}|$, and ρ_{22} can be neglected. It then follows that the steady solution for ρ_{12} and the polarization (6) oscillate at the incident frequency ω [31]. To find this solution, we can simulate optical response of a system for specific incident frequency ω. However, we can substantially save computing time with the help of short-pulse approach [31]. Following this approach, we specify an incident wave of the form of an ultrashort pulse. In the present simulations we use a Gaussian function, $E_{\rm inc}(t) = \exp\left[-(\frac{t-t_0}{t_w})^2\right]$, where the parameters t_0 and t_w are chosen to cover the considered spectral range. The impulse duration is $\sim$0.5 fs and the incident field strength is $\sim$1 V/m (we found that the optical response scales linearly with the incident intensity, as expected for the low field considered). The Maxwell-Liouville equations are evolved for several picoseconds (the simulation time should be longer than the lifetime of the excited state of the emitter $1/\gamma$). At the end of the simulation, we Fourier-transform the calculated field. We note that the incident pulse can be represented as a linear superposition of cw plane waves with different frequencies ω. Therefore, under the conditions of linear response (which is valid in our case of low incident intensity), the Fourier-transformed field $\mathbf{E}(\omega)$ contains all the information relevant to a steady state process at the frequency ω.

To simulate the incident pulse on a finite FDTD mesh, we apply the total field–scattered field (TF-SF) approach discussed in Sec. IIA: an incident wave is generated at the TF-SF border and propagates in the total field (TF) region; see red box (1) in Fig. 5. The total field is simulated within the TF region. Total field includes the incident field, the field produced by the polarized nanoparticles, and the field due to the excited quantum emitter. The field $E_x(t)$ substituted into the Liouville equations (24), (25) should be free of the quantum emitter primary radiation (8) in order to avoid self-interaction. This can be accomplished using one of the techniques described in Sec. II.

At the end of the simulation, we Fourier-transform the calculated field and normalize it by the incident field spectrum. The Poynting flux of this field is integrated over appropriately chosen surfaces to obtain the scattering and absorption cross

sections; see surfaces (2) and (3) in Fig. 5. The absorption spectrum can be also calculated as $\int_V \omega\,\mathrm{Im}(\varepsilon)|\mathbf{E}(\omega,\mathbf{r})|^2 d^3r$, where V is the volume of the nanoparticles. As we verified also numerically, both methods lead to the same result.

We impose boundary conditions in the form of convolution perfectly matched layers (PMLs) [22] to avoid numerical reflection of outgoing electromagnetic wave back into the simulation domain. To minimize undesired numerical reflection from the PMLs we use additional back-absorbing layers [61] (this technique is especially effective for evanescent waves).

Simulation of the metal nanoparticles requires special care to ensure proper description on the rectangular FDTD mesh. This is accomplished by means of a subpixel smoothing method for dispersive media [62], which significantly improves the FDTD accuracy for arbitrarily shaped scatterers. Experimental data for the gold dielectric permittivity $\varepsilon(\omega)$ are taken from [63,64]. The frequency dependence of $\varepsilon(\omega)$ is assigned using the modified Lorentz approximation, within which the dielectric polarization depends on both the electric field and its first time derivative [65,66],

$$\varepsilon(\omega) = \varepsilon_\infty - \frac{\omega_D^2}{\omega^2 + i\omega\gamma_D} + \sum_{p=1}^{2} \frac{\Delta\varepsilon_p\left(\omega_p^2 - i\gamma_p'\omega\right)}{\omega_p^2 - 2i\omega\gamma_p - \omega^2}, \quad (26)$$

with $\varepsilon_\infty = 1.14$, $\omega_D = 7$, $\gamma_D = 0.057$, $\Delta\varepsilon_1 = 0.23$, $\Delta\varepsilon_2 = 4.48$, $\omega_1 = 2.07$, $\omega_2 = 2.54$, $\gamma_1 = 0.237$, $\gamma_2 = 1.25$, $\gamma_1' = 4.5$, $\gamma_2' = 2.71$; ω_D, γ_D, ω_p, γ_p, and γ_p' are given in $1/\mu$m units, and the speed of light is unity. The modified Lorentz approximation is implemented in the simulation using the auxiliary differential equation (ADE) technique [65].

The dashed curves in Fig. 6 show the scattering and absorption cross sections for the system of two ellipsoids without the quantum emitter. Results obtained using both approaches described in Sec. II are in good agreement (the difference between then is indistinguishable in Fig. 6). The field-partitioning approach requires reservation of the additional free space around the quantum emitter for the internal TF region (see small red box in Fig. 5). As discussed in Sec. II A, this space should be at least 5 mesh steps, which places a lower bound on the separation between the gold ellipsoids. If the distance between ellipsoids is smaller (a few mesh steps), the symmetry-adapted averaging approach can be applied, or the mesh resolution can be increased to make the field-partitioning approach applicable.

As expected, the calculated spectra exhibit a strong longitudinal dipolar plasmon resonance at a frequency $\omega = 1.7$ eV, where the electric field $\mathbf{E}(\omega)$ is greatly enhanced as compare to its incident value (Fig. 6, inset). Field enhancement is a characteristic feature of localized surface plasmons with a wide variety of applications [3]. The solid curves of Fig. 6 illustrate the corresponding cross section spectra for a pair of ellipsoids separated by a quantum emitter. The dipole moment is taken to be $\mu = 3\,e$ nm, the dissipation rates are $\gamma = 10^{11}$ s^{-1} and $\gamma^* = 2 \times 10^{11}$ s^{-1}, and the transition frequency is tuned to the frequency of a plasmon resonance, $\omega_0 = 1.7$ eV. We observe a deep transparency minimum in the calculated spectra, caused by Fano interference between the plasmon resonance and the quantum emitter transition. A similar phenomenon was found in the previous literature [10], where the quantum emitter (quantum dot) was modeled using a dielectric function as a single Lorentz term [10,67–69]. This latter model is valid only in the low excitation limit, where quantum-mechanical coherences between the ground and excited states of a quantum emitter can be neglected, a condition that is satisfied at the intensity considered in [10] and in the present study. In our future work we plan to apply the present (nonperturbative) model to study the interaction between a quantum emitter and a plasmon subject to nonlinear interaction with incident fields.

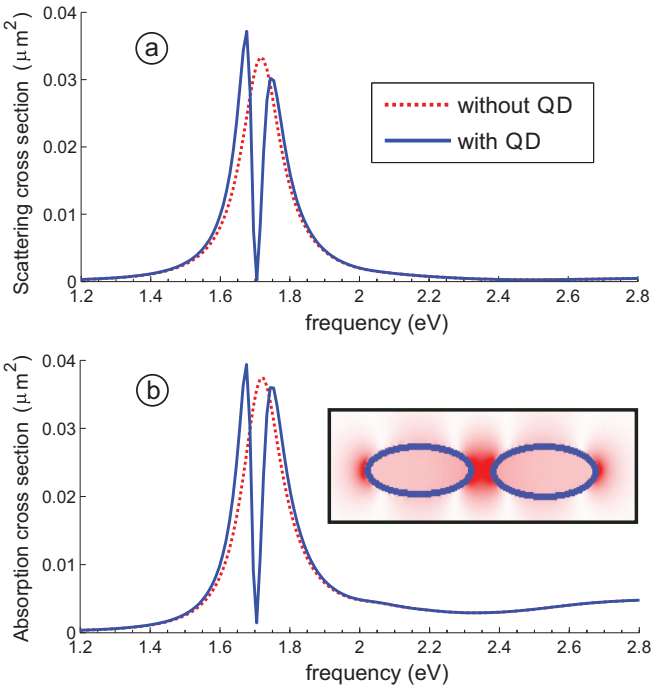

FIG. 6. (Color online) Scattering (a) and absorption (b) cross section for a system of two gold ellipsoids (major diameter 80 nm, minor diameter 30 nm, distance between ellipsoids 15 nm), subject to an incident light field polarized in the horizontal direction. The dashed curves in both figures are computed for the bare plasmonic system whereas the solid curves are obtained in the presence of a quantum emitter between the ellipsoids, resulting in a transparency minimum in both spectra (transition frequency $\omega_0 = 1.7$ eV, dipole moment $\mu = 3\,e$ nm, relaxation rates $\gamma = 10^{11}$ s^{-1}, $\gamma^* = 2 \times 10^{11}$ s^{-1}). The inset shows the field distribution (component parallel to the incident light polarization) at frequency $\omega = 1.7$ eV in the absence of the quantum emitter. Different scales are used for the vertical and horizontal dimensions.

IV. CONCLUSION

In this paper we developed two finite-difference time domain (FDTD) approaches for simulation of single quantum emitters interacting with plasmonic nanoparticles. Both approaches are designed to eliminate the problem of self-interaction, which often appears spuriously in solutions of the coupled Maxwell-Liouville equations. Hence both approaches can be used for modeling of single as well as ensembles of quantum emitters in arbitrary dielectric environment.

One approach is based on a field-partitioning concept, akin to the familiar total field–scattered field technique for simulation of point-source radiation. The second approach is

based on field averaging at a specifically chosen (symmetry adapted) set of points around the emitter. We illustrated the accuracy and efficiency of the methods by application to two problems, both of which are fundamentally and practically interesting while also providing complementary tests of the accuracy of the methods. One application, Sec. III A, is the calculation of spontaneous emission rates. Here, by considering an analytically soluble model, we were able to show that the field-partitioning method yields perfect agreement with the exact (analytical) solution, whereas the symmetry-adapted averaging method is somewhat less accurate but has the merits of simplicity and elegance. Both of these findings were anticipated. As a second application, we explored the interaction of a single quantum emitter (e.g., quantum dot) with metal nanoparticles, a problem that is the topic of ongoing experiments with interesting potential applications. We compared the proposed approaches with the standard method of solving the coupled Maxwell-Liouville equations (within which the primary emitter radiation can influence its dynamics) and discussed implications.

Our approaches exhibit all the advantages of the FDTD method: they are suitable for simulation of nanoparticles with arbitrary geometry and optical properties (dispersion, anisotropy, nonlinearity), and they can be easily used for observation of the field evolution in time and space. The proposed approaches are relatively simple to program and can be readily incorporated into an existing FDTD code.

Our approaches can be applied to a variety of interesting topics, including the interaction of plasmons with multiple quantum emitters, the interaction of a quantum emitter with dark plasmons, and the new physics introduced under nonperturbative fields. These problems are the subjects of ongoing research in our group.

ACKNOWLEDGMENTS

We thank the National Science Foundation (Grant No. CHE-1012207/001) and the Department of Energy (Grant No. DE-SC0001785) for support of the research described in this article.

[1] J. Homola, S. S. Yeea, and Gunter Gauglitz, Sens. Actuators, B **54**, 3 (1999).
[2] K. A. Willets and R. P. Van Duyne, Annu. Rev. Phys. Chem. **58**, 267 (2007).
[3] S. Zalyubovskiy, M. Bogdanova, A. Deinega, Yu. Lozovik, A. Pris, K. H. An, W. Paige Hall, and R. A. Potyrailo, J. Opt. Soc. Am. A **29**, 994 (2012).
[4] L. Novotny and B. Hecht, *Principles of Nanooptics* (Cambridge University Press, Cambridge, 2011).
[5] Y. Xu, R. K. Lee, and A. Yariv, Phys. Rev. A **61**, 033807 (2000).
[6] V. Giannini, J. Sanchez-Gil, O. Muskens, and J. G. Rivas, J. Opt. Soc. Am. B **26**, 1569 (2009).
[7] X. Wu, Y. Sun, and M. Pelton, Phys. Chem. Chem. Phys. **11**, 5867 (2009).
[8] W. Zhang, A. O. Govorov, and G. W. Bryant, Phys. Rev. Lett. **97**, 146804 (2006).
[9] R. Artuso and G. Bryant, Nano Lett. **8**, 2106 (2008).
[10] X. Wu, S. Gray, and M. Pelton, Opt. Exp. **18**, 23633 (2010).
[11] S. Savasta, R. Saija, A. Ridolfo, O. Di Stefano, P. Denti, and F. Borghese, ACS Nano **4**, 6369 (2010).
[12] A. Manjavacas, F. J. Garcia de Abajo, and P. Nordlander, Nano Lett. **11**, 2318 (2011).
[13] R. A. Shah, N. F. Scherer, M. Pelton, and S. K. Gray, Phys. Rev. B **88**, 075411 (2013).
[14] D. Englund, A. Faraon, I. Fushman, N. Stoltz, P. Petroff, and J. Vuckovic, Nature (London) **450**, 857 (2007).
[15] S. Sadeghi, J. Nanotechnol. **20**, 225401 (2009).
[16] S. M. Sadeghi, Phys. Rev. B **79**, 233309 (2009).
[17] R. D. Artuso and G. W. Bryant, Phys. Rev. B **82**, 195419 (2010).
[18] K. Lopata and D. Neuhauser, J. Chem. Phys. **130**, 104707 (2009).
[19] K. Lopata and D. Neuhauser, J. Chem. Phys. **131**, 014701 (2009).
[20] J.-Y. Yan, W. Zhang, S. Duan, X.-G. Zhao, and A. Govorov, Phys. Rev. B **77**, 165301 (2008).
[21] R. D. Artuso, G. W. Bryant, A. Garcia-Etxarri, and J. Aizpurua, Phys. Rev. B **83**, 235406 (2011).
[22] A. Taflove and S. H. Hagness, *Computational Electrodynamics: The Finite Difference Time-Domain Method* (Artech House, Boston, 2005).
[23] R. W. Ziolkowski, J. M. Arnold, and D. M. Gogny, Phys. Rev. A **52**, 3082 (1995).
[24] G. Slavcheva, J. M. Arnold, I. Wallace, and R. W. Ziolkowski, Phys. Rev. A **66**, 063418 (2002).
[25] J. Gruetzmacher and N. Scherer, Opt. Lett. **28**, 573 (2003).
[26] F. Schlottau, M. Piket-May, and K. Wagner, Opt. Express **13**, 182 (2005).
[27] Y. Niu, K. Xia, N. Cui, S. Gong, and R. Li, Phys. Rev. A **78**, 063835 (2008).
[28] A. Fratalocchi, C. Conti, and G. Ruocco, Phys. Rev. A **78**, 013806 (2008).
[29] B. Bidegaray, Numer. Methods Partial Differ. Equ. **19**, 284 (2003).
[30] A. Bourgeade and O. Saut, J. Comput. Phys. **213**, 823 (2006).
[31] M. Sukharev and A. Nitzan, Phys. Rev. A **84**, 043802 (2011).
[32] A. Salomon, R. J. Gordon, Y. Prior, T. Seideman, and M. Sukharev, Phys. Rev. Lett. **109**, 073002 (2012).
[33] M. Sukharev and S. A. Malinovskaya, Phys. Rev. A **86**, 043406 (2012).
[34] E. Charron and M. Sukharev, J. Chem. Phys. **138**, 024108 (2013).
[35] S.-H. Chang and A. Taflove, Opt. Express **12**, 3827 (2004).
[36] P. Bermel, E. Lidorikis, Y. Fink, and J. D. Joannopoulos, Phys. Rev. B **73**, 165125 (2006).
[37] S. Shi and D. Prather, Opt. Express **15**, 10294 (2007).
[38] B. Redding, S. Shi, T. Creazzo, and D. W. Prather, Opt. Express **16**, 8792 (2008).
[39] A. Fang, T. Koschny, and C. Soukoulis, J. Opt. **12**, 024013 (2010).

[40] M. Tatsunosuke and K. Masahiro, Appl. Phys. Express **3**, 061701 (2010).
[41] C. Arntsen, K. Lopata, M. Wall, L. Bartell, and D. Neuhauser, J. Chem. Phys. **134**, 084101 (2011).
[42] I. Valuev, A. Deinega, and S. Belousov, Opt. Lett. **33**, 1491 (2008).
[43] I. Valuev, A. Deinega, and S. Belousov, Comput. Phys. Commun. (2014), http://dx.doi.org/10.1016/j.cpc.2014.01.001.
[44] A. Aminian and Y. Rahmat-Samii, IEEE Trans. Antennas Propag. **54**, 1818 (2006).
[45] Y.-J. Zhou, X. Zhou, T.-J. Cui, R. Qiang, and J. Chen, Prog. Electromagn. Res. M **17**, 101 (2011).
[46] A. Deinega, S. Belousov, and I. Valuev, Phys. Rev. E **88**, 053305 (2013).
[47] J.-P. Berenger and A. Huygens, IEEE Trans. Antennas Propag. **54**, 3797 (2006).
[48] Z. Hu, M. Ratner, and T. Seideman, J. Chem. Phys. **137**, 204111 (2012).
[49] Z. Huang, G. G. Pan, K.-S. Chen, IEEE Trans. Antennas Propag. **61**, 2605 (2013).
[50] J. Schneider, IEEE Trans. Antennas Propag. **52**, 3280 (2004).
[51] C. M. Bowden and J. P. Dowling, Phys. Rev. A **47**, 1247 (1993).
[52] G. Grynberg, A. Aspect, and C. Fabre, *Introduction to Quantum Optics: From the Semiclassical Approach to Quantized Light* (Cambridge University Press, Cambridge, 2010).
[53] Electromagnetic Template Library (EMTL), Kintech Lab Ltd., http://fdtd.kintechlab.com.
[54] Y. Xu, J. Vuckovic, R. Lee, O. Painter, A. Scherer, and A. Yariv, J. Opt. Soc. Am. B **16**, 465 (1999).
[55] A. F. Koenderink, M. Kafesaki, and C. M. Soukoulis J. Opt. Soc. Am. B **23**, 1196 (2006).
[56] C. Hermann and O. Hess, J. Opt. Soc. Am. B **19**, 3013 (2002).
[57] C. Van Vlack and S. Hughes, Opt. Lett. **37**, 2880 (2012).
[58] J.-F. Chen, R.-T. Hong, and J.-Y. Yang, J. Appl. Phys. **107**, 023110 (2010).
[59] W. Vos, A. F. Koenderink, and I. Nikolaev, Phys. Rev. A **80**, 053802 (2009).
[60] E. Hairer, S. P. Norsett, and G. Wanner, *Solving Ordinary Differential Equations*, 2nd rev. ed. (Springer-Verlag, Berlin, 1993), Springer Series in Computational Mathematics, Vols. 8, 14.
[61] A. Deinega and I. Valuev, Comput. Phys. Commun. **182**, 149 (2011).
[62] A. Deinega and I. Valuev, Opt. Lett. **32**, 3429 (2007).
[63] P. Johnson and R. Christy, Phys. Rev. B **6**, 4370 (1972).
[64] A. Vial, T. Laroche, M. Dridi, and L. Le Cunff, Appl. Phys. A **103**, 849 (2011).
[65] A. Deinega and S. John, Opt. Lett. **37**, 112 (2012).
[66] See http://fdtd.kintechlab.com/en/fitting.
[67] Y. Zeng, Y. Fu, M. Bengtsson, X. Chen, W. Lu, and H. Agren, Opt. Express **16**, 4507 (2008).
[68] H. Taniyama, H. Sumikura, and M. Notomi, Opt. Express **19**, 23067 (2011).
[69] J. Llorens, I. Prieto, L. Munioz-Camuniez, and P. Postigo, J. Opt. Soc. Am. B **30**, 1222 (2013).